ORIGINAL ARTICLE

Embedded System for the Analysis of Thermal Properties of Hemoglobin

Alejandro Castañeda-Miranda[1] · Víctor M. Castaño[2]

Abstract
A novel embedded photoacoustic system design is described and a calculation method is proposed to determine the blood hemoglobin oxygen saturation through the thermal properties of different skin color types. A heat equation model allows a calculation procedure to determine the reflection and transmitted thermal wave amplitude for obtaining a depth profile, depending on the modulation frequency at the air-skin-subcutaneous tissue interface. Our reflection-mode photoacoustic technique involves the use of a 445 nm pulsed-laser light spot on subcutaneous tissue to obtain amplitude and phase from signals for different skin color types. The transmission and reflection temperature coefficients are fitted through a heat propagation model to estimate the thermal wave properties of blood hemoglobin. Nonlinearly amplified photoacoustic signals are modeled from the microphone and their stability analyzed by a bode diagram, as to consider overheated hemoglobin background. An dedicated electronic embedded system is thus integrated, including memory, processor and preprocessor, to provide a simple measurement technique, as compared to conventional instruments.

Keywords Reflection-mode photoacoustic · Hemoglobin thermal properties · Nonlinearly amplified system

Introduction

PhotoAcoustic Photothermal (PAP) techniques have drawn attention for the thermal characterization of semiconductors [1], metals [2], and organic materials [3] and their most recent application is in biomedical technology [4]. Photoacoustic Photothermal Infrared leads the Photothermal techniques mainly because of its non-destructive, remote, non-contact nature and since it allows the analysis of samples online at low cost, given the sensor is basically a microphone. These instruments are now employed for various applications, including the natural gas industry [5], airborne hygrometry [6], source apportionment of urban light-absorbing aerosols [7], measurements of gas permeability [8], and clinical research [9]. The Data Acquisition and Control System (DACS) has a fundamental role in a PAP system, for it drives the laser: tunes and stabilizes its wavelength and modulates its emitted light [10] which requires a good knowledge of the ranges and modes of operation of electronic devices used in embedded systems. The PAP technique has allowed non-destructive developments in engineering [11] and biological materials [12], as the recent advances in the kinetic measurements for ferritin decomposition at high pH's [13]. Upon comparing their images with the profile of the dislocation density, they concluded that the radiometric signal was generated by non-radioactive phenomena and was sensitive to even low densities. Sweeps in frequency, were subsequently used for materials analysis as an alternative to purely thermal techniques that had been used for some time for analyzing homogeneity of nanoscale temperatures [14] and thermal parameters in implants, including surface damage [15]. The black body emission was associated mainly to photonic excited states and the thermal contribution is compared with spectrophotometry at lower concentrations and show good reproducibility and accuracy of kinetic

✉ Alejandro Castañeda-Miranda
    alejandro.castaneda@uteq.edu.mx

✉ Víctor M. Castaño
    vmcastano@unam.mx

1   Environmental Technology Division, Creativity
    and Innovation Center 4.0, Universidad Tecnológica de
    Querétaro (CIC 4.0-UTEQ), Av. Pie de la Cuesta 2501,
    Nacional, 76148 Santiago de Querétaro, Querétaro, Mexico

2   Centro de Física Aplicada y Tecnología Avanzada,
    Universidad Nacional Autónoma de México, Boulevard
    Juriquilla 3001, 76230 Santiago de Querétaro, Querétaro,
    Mexico

constants [16]. Currently, this measurement technique also uses computer-simulation studies for far-field-based imaging for 3D PACT small animals imaging system [17]. In a blood sample the photoacoustic detection of single absorbing targets, such as nanoparticles or cells, can be limited by background absorption, this problem can be overcome by using nonlinear photoacoustic based on the differences between the laser energy and the background surface emission. This, however, makes the detection problematic for in vitro tests, where only a limited volume (few mL) of blood can be tested [18]. A reflection-mode multiple-illumination photoacoustic method allows to estimate optical scattering properties of turbid media based on fitting light-transport models and explore its limits in optical property estimation and depth-dependent fluency compensation [19].

For obtaining blood thermal properties in hand finger there are several methods: one is the generation of photoacoustic signals for imaging objects embedded within tissues, which is dependent on how well light can penetrate within an optically absorbing object, such as a blood vessel, where a limit is the sophistication of the stress wave calculation and no attempt to properly account for changes in the sound velocity of different tissue types has been reported [20]. From the point of view of instrumentation software an important recent development is the use of embedded systems: the software for measurement and test applications has been divided into two main distinct groups of solutions related to the scenario on the market and to the state of the art in research [21]. The embedded devices have gradually increased the demand for computing performance and adaptive load scheduling algorithm has been designed, and real-time scheduling, by blocking and queueing the situation of each core the approximate iterative algorithm, has been proposed for evaluating system performance [22]. A methodology for choosing the appropriate measurement oriented software focuses on the use of mathematical modeling for the analysis, design and soft measurement systems, especially through measurement sub-systems in the form of instruments and instrument elements [23]. A methodology for embedded software consists in the use of quantitative algebra of a measured system and that of a measuring instrument, underlying the causal linkages in classical system instrument interactions [24]. These tools, which use artificial intelligence software, give rise to novel application fields such as fuzzy optical as is the use of a predictive method, based on artificial neural network to study absorbance and pH effects on the equilibrium of blood serum [25], but unfortunately the thermal wave part has not been considered, only attempting to model pressure waves generated in superficial brain tissue that escapes through the skull. To produce an effective topical detector requires to model changes in attenuation and sound velocity through the skull, and to model reflected pressure waves internally reflecting from the air/skin surface and encountering the skin/skull and skull/brain interfaces to reflect backwards to the detector. One aspect to consider when developing instruments is to consider that an usable measurement system has to be non-invasive, user friendly and portable [26]. Unfortunately, if the microphone instrument is uncharacterized, the possibility of employing an all-frequency domain for experimental measurements as a function of noise is limited. Some modeling uses the Green's function solution to the pressure wave equation in frequency domain and the resulting inverse problem is solved using regularized least squares minimization [27]. If the instrument is characterized from the electronic part, building on its high spatial resolution and deep penetration depth in principle one can achieve up to 100% relative sensitivity to optical absorption and its ultimate detection sensitivity is limited only by thermal noise [28].

Materials and Methods

Two methods were used for the PAP experiments, the first is the periodic measurement of samples, to obtain a time spectrum through Fourier transform [29]. The instrument used it is a spectrum analyzer and its disadvantage is the spatial resolution and the device allowed for measurements at frequency range between 1 MHz and 100 kHz [30]. The second method is to produce a reference signal that serves both for modulating and for demodulating the signal, obtaining the amplitude and phase, which are associated with the radiation interaction with matter and is conducted through an locking amplifier, capable of providing high frequency selectivity, thus allowing the user to distinguish an interesting signal from the background noise, and has become an important component in the instrumentation for the study of many different physical phenomena [31] As for the thermal measurement instruments, a comparison of photo pyroelectric calorimetry and infrared lock-in thermography was done [32]. The experimental components employed are a blue laser source at 445 nm, 5 mW output power FDA Class IIIa, a microphone detector which allows collecting the photoacoustic signal (SPA[$\omega 0$]) from the blood hemoglobin of the hand finger. The arrangement is shown in Fig. 1, where a modulated beam impinges on the finger, from which a relation between modulation frequency and deep profile is obtained. The signal from absorbance is collected through a microphone. Finally, the signal is analyzed in the frequency domain, assigning a fundamental frequency and its possible harmonics.

Experimental Measurement Arrangement consists of two parts, the first is the electronics and embedded software part, where the laser beam modulation is controlled through a chopper, which transforms a PWM signal rotation of the DC motor shaft and interrupts periodically the

Fig. 1 Scheme systems using to determine the hemoglobin in red blood cells thermal properties
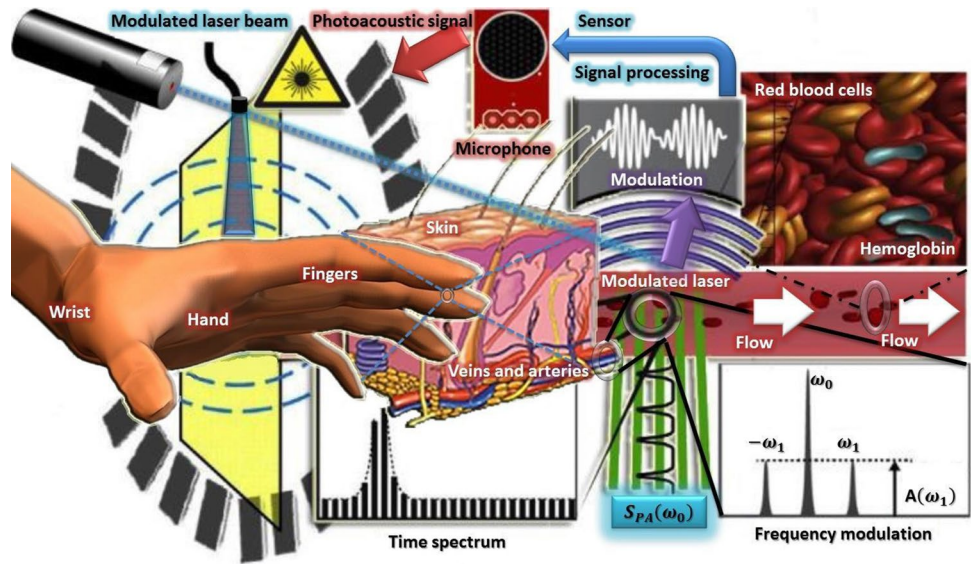
laser intensity. This modulated radiation impinges normally on hand finger, blue optical radiation interacting with the skin is transformed into thermal radiation, which becomes a thermal wave reflected from skin surface and subcutaneous tissue sub-surface. Nevertheless, this wave interacts with veins and red blood cells, obtaining thermal wave properties in blood hemoglobin, this pressure wave is collected through a microphone that is mounted normal to the finger surface and in parallel with the laser beam. The microphone captured the signal, which is pre-amplified and passed through an instrumentation amplifier (Texas Instruments INA128p), to be demodulated by a lock-in amplifier (Analog Devices AD630), the amplitude and phase signal is preprocessed by a microcontroller (PJRC

Store Teensy 3.2) and processed in a processor (Intel Edison). Moreover, preprocessor a PWM signal is created to synchronize the motor with the tuned frequency for measurement system phase sensitive amplifier the experimental measurement arrangement is show in Fig. 2. In Fig. 2 a modulated beam, using a perforated disk ($10 \cdot \omega_0$) and the PWM technique, strikes the finger, so the region of veins and arteries inside the finger under study is penetrated. The signal is collected by a microphone, to be amplified and analyzed in the frequency domain, by means of an embedded electronic system. For this particular case, a mechanical clamp prototype type used to hold the laser clamping finger and microphone arrangement according to experimental development measurement, the components of this mechanical hand finger clamp shown in Fig. 3.

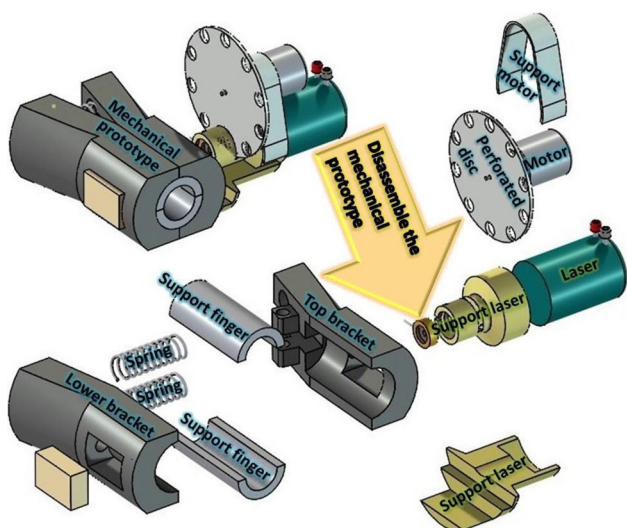**Fig. 2** Electrical and electronical scheme of experimental measurement arrangement
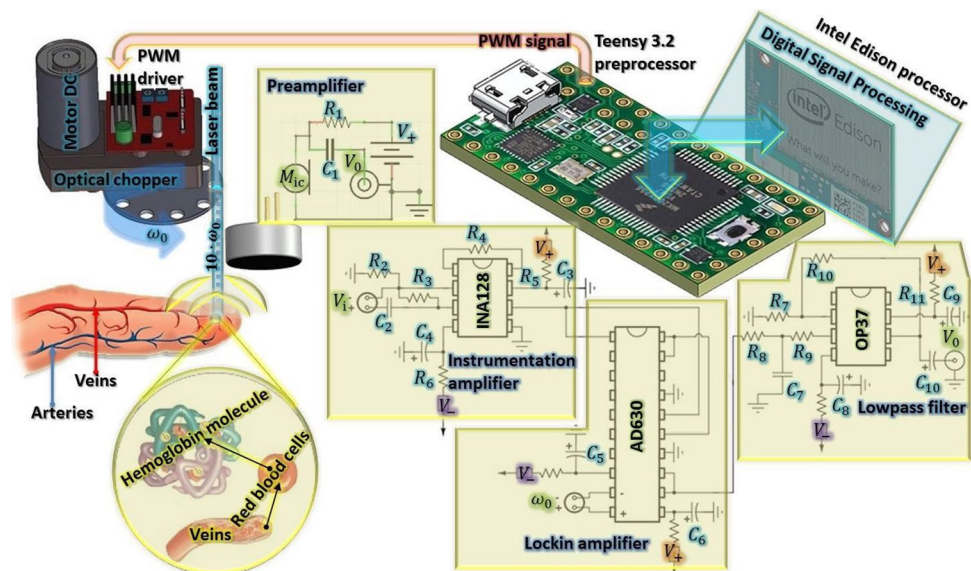
Fig. 3 Mechanical hand finger clamp components scheme and prototype mechanical assembly

Blood Hemoglobin Quantitative Aspects

Hemoglobin is a protein in red blood cells that carries oxygen; normal results for adults vary, but generally are for Man has a range from 13.8 to 17.2 g per deciliter and Women have a range of 12.1–15.1 g per deciliter. In the case of normal outcomes for children they vary but are generally in the case of newborn ranging from 14 to 24 g per deciliter and baby has a range of 9.5–13 g per deciliter. The importance in measuring hemoglobin level is that being a low measurement may be due to health problems such as anemia due to destruction of red blood cells earlier than normal (hemolytic anemia) or anemia in general (various types) [33], bleeding from the digestive tract or bladder; heavy menstrual periods, chronic kidney disease, bone marrow cannot produce new blood cells this may be due to leukemia, other cancers, drug toxicity, radiation, infection or bone marrow disorders, poor nutrition, low iron, folate, vitamin B12 and vitamin B6 and other chronic diseases, such as rheumatoid arthritis [34]. The hemoglobin high level is almost always due to low oxygen levels in the blood (hypoxia) [35], present for a time long period. Common reasons include certain congenital heart defects present at birth (congenital heart disease), failure of the heart right side, severe chronic obstructive pulmonary disease, scarring or lungs thickening (pulmonary fibrosis) and other serious lung disorders [36], other reasons for the hemoglobin high level include a bone rare disease that leads to an abnormal increase in the blood cells number and that the body does not have much water and fluids as it should (dehydration). The problem now is that the measurement method is invasive and is called blood gas analysis [37], consists inserting a needle into a vein to draw blood, being generally a painful method for the patient and depends on the physician experience to detect blood pressure, the risks of using invasive methods are due to as veins and arteries vary in size from one patient to another and from one body side to another, why obtain a blood sample from some people may be more difficult than from other, other risks associated with having blood drawn are slight but may be excessive bleeding, fainting or dizziness, generating hematoma (blood accumulation under the skin) and infection (a slight risk any time they present skin breakdown).

Heat Equation Model

From Fig. 4 let V be an arbitrary volume lying within a given material and let S denote its surface. Now let Φ (z, t) be the material temperature. Φ is a position and time function and is a complex for computational convenience. The heat flux across S is the heat leaving quantity V per unit of time and is defined by Eq. (1).

$$\iint_S -(thermal \cdot conductivity)(temperature \cdot gradient)dS$$
$$= -\iint_S \kappa \nabla \Phi \cdot \vec{n} dS \tag{1}$$

From Eq. (1) this is heat quantity entering V trough S per unit time, using the divergence theorem and this surface integral is converted into the volume integral and obtain the Eq. (2).

$$\iint_S \kappa \nabla \Phi \cdot \vec{n} dS = \iiint_V \nabla(\kappa \nabla \Phi)dV \tag{2}$$

On the other hand, in Fig. 4 the heat energy contained in V equals is written as Eq. (3).

$$\iiint_V (specific \cdot heat)(density)(temperature)dV = \iiint_V (c\rho\Phi)dV \tag{3}$$

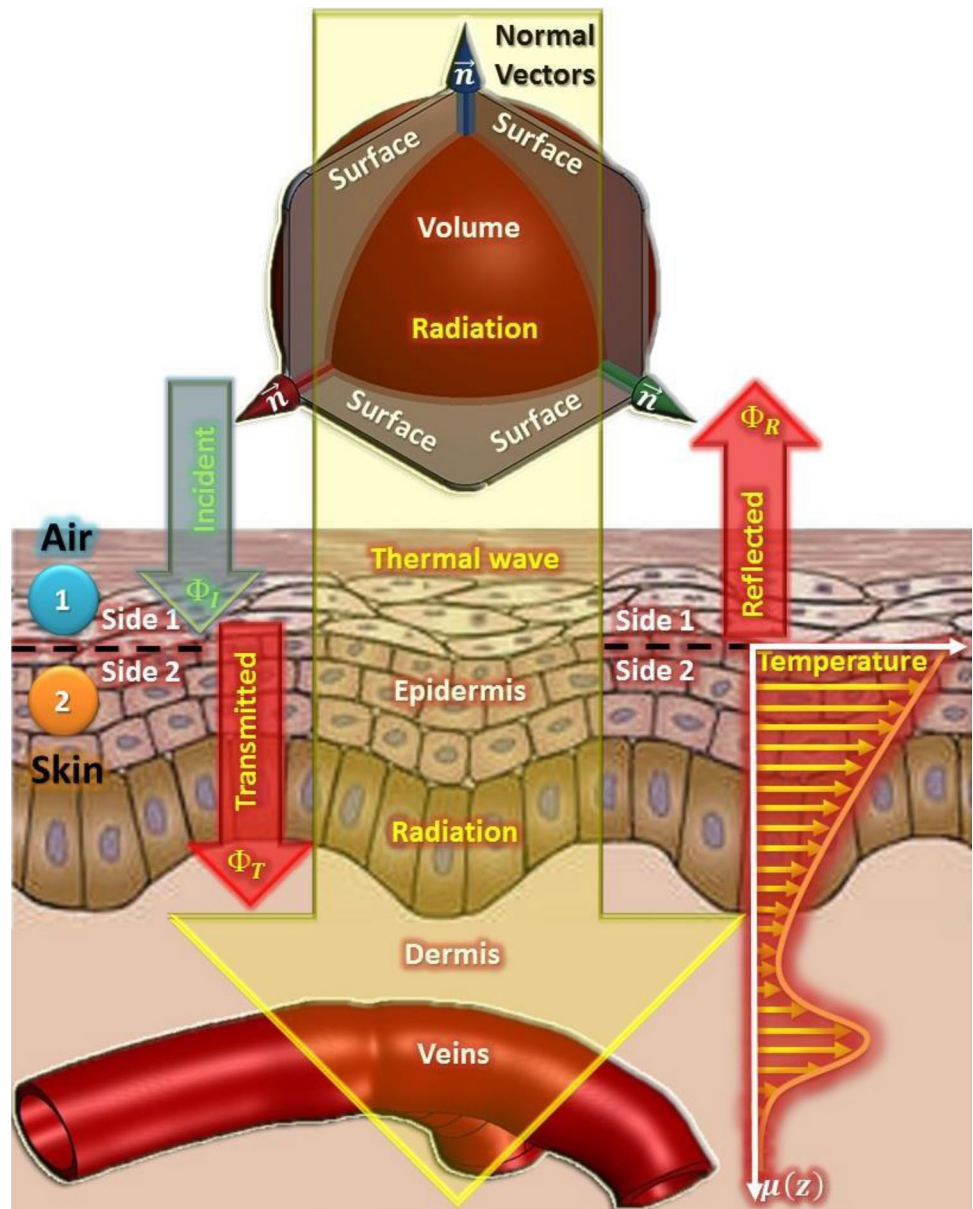From Eq. (3) where c is the specific heat and ρ is the density and then the heat rate in S is given by Eq. (4).

$$\frac{d}{dt} \iiint_V (c\rho\Phi)dV = \iiint_V \left(c\rho\frac{d\Phi}{dt}\right)dV \tag{4}$$

Combining Eqs. (2) and (4), the Eqs. (5) and (6) is obtained.

$$\iiint_V \nabla(\kappa \nabla \Phi)dV = \iiint_V c\rho\left(\frac{d\Phi}{dt}\right)dV \tag{5}$$

$$\iiint_V \left[\nabla(\kappa \nabla \Phi) - c\rho\left(\frac{d\Phi}{dt}\right)\right]dV = 0 \tag{6}$$

Fig. 4 Heat flow transmittance on surface and thermal wave incident on skin schematic

For an isotropic thermal conductivity κ and considering V an arbitrary volume, the Eqs. (7) and (8) is obtained.

$$\kappa \nabla^2 \Phi = c\rho\left(\frac{d\Phi}{dt}\right) \tag{7}$$

$$\frac{d^2\Phi}{dz^2} = \frac{c\rho}{\kappa}\left(\frac{d\Phi}{dt}\right) \tag{8}$$

From Eq. (8), one solution is written as Eq. (9), where f is frequency and Γ is a constant.

$$\Phi = \Gamma \cdot e^{-z(1+i)\sqrt{\frac{c\rho\pi \cdot f}{\kappa}}} \cdot e^{i\omega \cdot t} = \Gamma \cdot e^{-z(1+i)\sqrt{\frac{\pi \cdot f}{\alpha}}} \cdot e^{i\omega \cdot t}$$
$$= \Gamma \cdot e^{-\left[\frac{(1+i)}{\mu}\right]z} \cdot e^{i\omega \cdot t} = \Gamma \cdot e^{-\sigma \cdot z} \cdot e^{i\omega \cdot t} \tag{9}$$

The representation of Eq. (9) is called thermal wave, the amplitude damped is $\Gamma \exp(-z\sqrt{f})$, a part oscillating in space $\Gamma \exp[-i(z\sqrt{f})]$ and a part oscillating in the time $\exp(i\omega t)$. The part oscillating wavelength in space is called thermal wave. The thermal wave amplitude after one thermal wavelength is inconveniently small, so the thermal diffusion length ($\mu[z]$) is defined as $\sqrt{(\kappa/c\rho\pi f)}$ or $\sqrt{(\alpha/\pi f)}$, the amplitude is comparable 37% of the starting amplitude. In Fig. 4, as a light source falls upon a skin, the energy from the incident light at a given depth will initiate a thermal wave that will travel through the sample and repeatedly reflect between the sample boundaries. At each boundary a thermal wave fraction will be transmitted into the other medium, the thermal wave portion that is reflected and the portion that is transmitted are the incident and reflected waves on boundary side 1 and

the transmitted wave on boundary side 1 are described by Eqs. (10–12), respectively.

$$I = \Phi_I \cdot e^{-\sigma_1 \cdot z} \cdot e^{i\omega \cdot t} \tag{10}$$

$$R = \Phi_R \cdot e^{\sigma_1 \cdot z} \cdot e^{i\omega \cdot t} \tag{11}$$

$$T = \Phi_T \cdot e^{-\sigma_2 \cdot z} \cdot e^{i\omega \cdot t} \tag{12}$$

The one thermal wave temperature is present if exist the thermal wave amplitude, but more thermal waves temperatures are present if the amplitudes sum is obtained. The complex temperature on side 1 in Fig. 2 is described by Eq. (13).

$$T_{12} = \left(\Phi_I \cdot e^{-\sigma_1 \cdot z} + \Phi_R \cdot e^{-\sigma_1 \cdot z}\right) \cdot e^{i\omega \cdot t} \tag{13}$$

From Fig. 2, on side 2 the complex temperature is the Eq. (12), at the boundary between side 1 and side 2 in border $(z = 0)$, is represented by Eq. (14).

$$I_0 = \Phi_I \cdot e^{i\omega \cdot t}, R_0 = \Phi_R \cdot e^{i\omega \cdot t}, T_0 = \Phi_T \cdot e^{i\omega \cdot t} \tag{14}$$

On Eq. (14), applied the thermodynamics zeroth law in temperature continuity at the boundary is described by Eq. (15).

$$\Phi_I + \Phi_R = \Phi_T \tag{15}$$

In Fig. 4, by thermodynamics first law an energy conservation expression is heat going into the boundary must come out on the other side in the heat flux on both boundary sides must match. The heat flux is defined by Eq. (16), where A is the boundary area which will be the same on both sides sample.

$$heat \cdot flux = -\kappa \cdot A \cdot (dT / dz) \tag{16}$$

From Eq. (13) substituting in Eq. (16), the heat flux on side 1 is obtain the Eq. (17).

$$-\kappa_1 \cdot A \cdot \left\{ \frac{d\left[\left(\Phi_I \cdot e^{-\sigma_1 \cdot z} + \Phi_R \cdot e^{-\sigma_1 \cdot z}\right) \cdot e^{i\omega \cdot t}\right]}{dz} \right\}$$
$$= \kappa_1 \sigma_1 A \left(\Phi_I \cdot e^{-\sigma_1 \cdot z} - \Phi_R \cdot e^{-\sigma_1 \cdot z}\right) \cdot e^{i\omega \cdot t} \tag{17}$$

From Eq. (12) substituting in Eq. (16), the heat flux on side 1 is obtain the Eq. (18).

$$-\kappa_2 \cdot A \cdot \left\{ \frac{d\left(\Phi_T \cdot e^{-\sigma_2 \cdot z} \cdot e^{i\omega \cdot t}\right)}{dz} \right\} = \kappa_2 \sigma_2 A \cdot \left(\Phi_T \cdot e^{-\sigma_2 \cdot z} \cdot e^{i\omega \cdot t}\right) \tag{18}$$

In Eq. (15), substituting the results of Eqs. (17) and (18) in border $(z = 0)$, is defined the Eq. (19).

$$\kappa_1 \sigma_1 A \left(\Phi_I - \Phi_R\right) \cdot e^{i\omega \cdot t} = \kappa_2 \sigma_2 A \cdot \left(\Phi_T \cdot e^{i\omega \cdot t}\right),$$
$$\Phi_I - \Phi_R = \left(\frac{\kappa_2 \sigma_2}{\kappa_1 \sigma_1}\right) \cdot \Phi_T \tag{19}$$

Using Eqs. (15) and (19) to solve simultaneously by addition and subtraction, Eq. (20) it is obtained.

$$2 \cdot \Phi_I = \left(1 + \frac{\kappa_2 \sigma_2}{\kappa_1 \sigma_1}\right) \cdot \Phi_T,$$
$$\Phi_T = \left\{2 \Big/ \left[1 + \left(\frac{\kappa_2 \sigma_2}{\kappa_1 \sigma_1}\right)\right]\right\} \cdot \Phi_I = \left[\frac{2}{(1 + \xi_{12})}\right] \cdot \Phi_I \tag{20}$$

On Eq. (20), the effectivities radio (ξ_{12}) is described as a relationship between the interfaces, the transmission coefficient is defined as the wave amplitude radio transmitted to the incident wave amplitude in the boundary between side 1 and side 2 is defined by Eq. (21), where T12 is thermal wave transmitted side.

$$T_{12} = \frac{\Phi_T}{\Phi_I} = \frac{\left[2 \Big/ (1 + \xi_{12})\right] \cdot \Phi_I}{\Phi_I} = \frac{2}{(1 + \xi_{12})} \tag{21}$$

Substituting Eqs. (20) in (15), the Eq. (22) is obtained.

$$\Phi_I + \Phi_R = \left[\frac{2}{(1 + \xi_{12})}\right] \cdot \Phi_I,$$
$$\Phi_R = \left[\frac{2 - (1 + \xi_{12})}{1 + \xi_{12}}\right]$$
$$\cdot \Phi_I = \left(\frac{1 - \xi_{12}}{1 + \xi_{12}}\right) \cdot \Phi_I \tag{22}$$

In Eq. (22), the reflection coefficient R12 is defined as the wave amplitude reflected radio to the incident wave amplitude in the boundary between side 1 and side 2 is defined by Eq. (23).

$$R_{12} = \frac{\Phi_R}{\Phi_I} = \frac{\left[(1 - \xi_{12}) \Big/ (1 + \xi_{12})\right] \cdot \Phi_I}{\Phi_I} = \frac{(1 - \xi_{12})}{(1 + \xi_{12})} \tag{23}$$

From one medium surface 3, the thermal wave is partly reflected to reemerge into medium 2 and combined with the wave amplitude, since the phase is the same between side 2 and side 3, from Fig. 5 it can be calculated the phase retardation (β) by multiple reflections between the surfaces and is defined vector ally by Eq. (24), where the phase difference may appear a difference in the path length traversed by the two waves that are original and reflected, or by an initial phase difference.

$$\beta = 2 \cdot \hat{\kappa}_2 \cdot \vec{r}_2 - \hat{\kappa}_1 \cdot \vec{r}_1 = 2x\left(\hat{\kappa}_2 \cdot \hat{i} - \hat{\kappa}_1 \cdot \hat{i}\right) + 2d\hat{\kappa}_2 \cdot \hat{k}$$
$$= 2d(\omega / c)(p + iq) = 4\pi d\left[(p + iq) / \lambda\right] \tag{24}$$

Fig. 5 Diagram for thermal wave interference between three propagation means and its calculation for the phase difference (β)
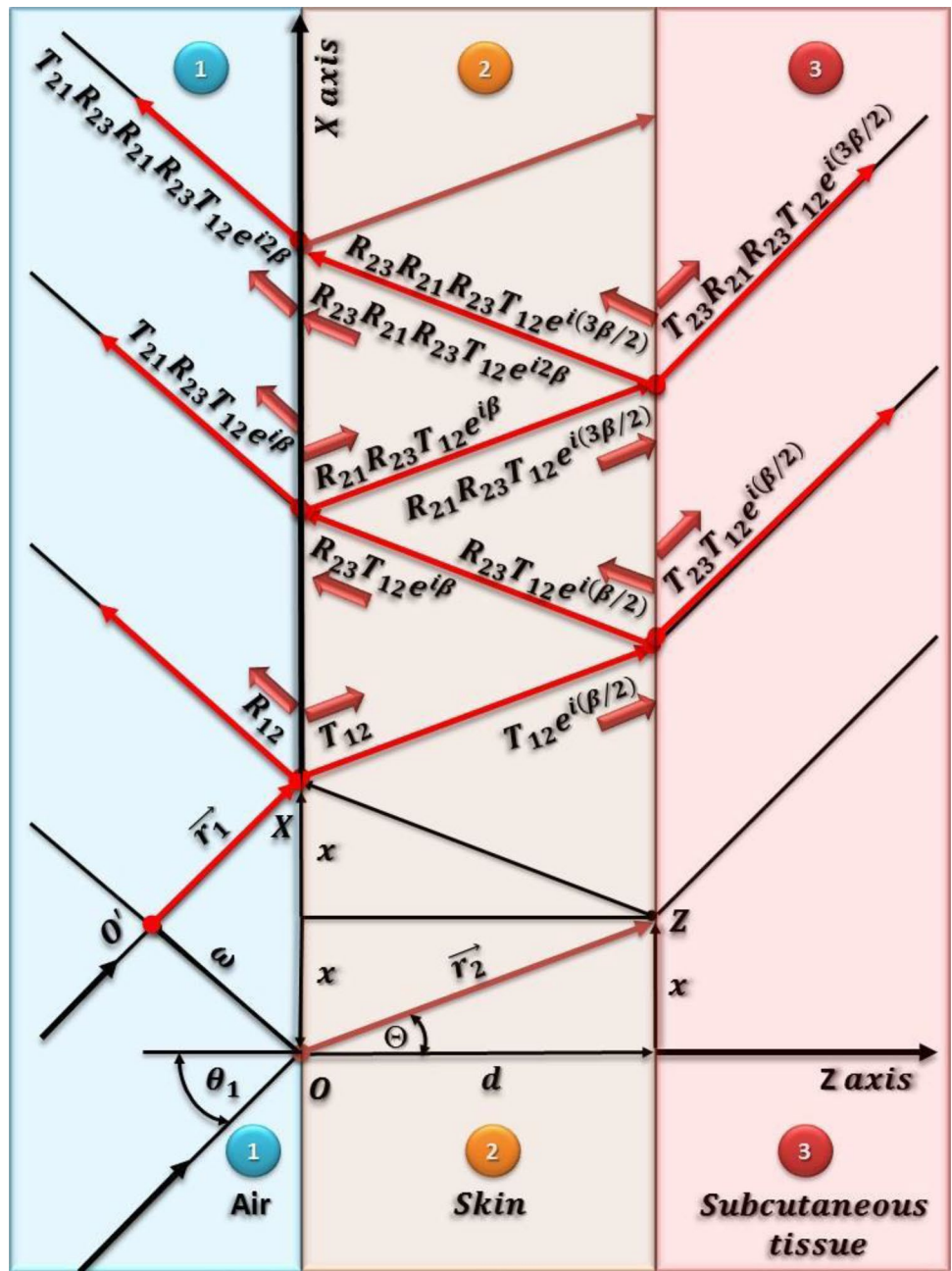
In Eq. (24), d is the thickness between interfaces face 2 and side 3; λ is the wavelength the incident radiation and p and q factors are calculated with Eq. (25), where δ is the skin depth at incidence normal.

$$e^{(1/2)i\hat{\beta}}e^{-(1/2)i\hat{\beta}^*} = e^{(1/2)i(\hat{\beta}-\hat{\beta}^*)} = e^{(d\omega/c)[(-q+ip)-(q+ip)]}$$
$$= e^{-2d(\omega/c)q} = e^{-2d/\delta} \quad (25)$$

In Fig. 5 for three interfaces the thermal wave amplitude for reflection from side 2 and side 3 is defined by Eq. (26).

$$R_T = R_{12} + T_{12}R_{23}T_{21}e^{i\hat{\beta}} + T_{12}R_{23}R_{21}R_{23}T_{21}e^{i2\hat{\beta}}$$
$$+ T_{12}R_{23}R_{21}R_{23}R_{21}R_{23}T_{21}e^{i3\hat{\beta}} + ...$$
$$R_T = R_{12} + T_{12}R_{23}T_{21}e^{i\hat{\beta}} \quad (26)$$
$$\left[1 + R_{21}R_{23}e^{i\hat{\beta}} + \left(R_{21}R_{23}e^{i\hat{\beta}}\right)^2 + \left(R_{21}R_{23}e^{i\hat{\beta}}\right)^3 + ...\right]$$

The mathematical series sums are represented by the Eq. (27).

$$1 + a + a^2 + a^3 + a^4 + \ldots = 1/(1-a) \tag{27}$$

Of the Eq. (26) using the series of Eq. (27), the Eq. (28) is obtained.

$$R_T = R_{12} + \frac{T_{12}R_{23}T_{21}e^{i\hat{\beta}}}{1 - R_{21}R_{23}e^{i\hat{\beta}}} = \frac{R_{12} + R_{23}(T_{12}T_{21} - R_{21}R_{21})e^{i\hat{\beta}}}{1 - R_{21}R_{23}e^{i\hat{\beta}}} \tag{28}$$

In energy balance place at the interface between two media (R+T=1), the Eqs. (29) and (30) is represented.

$$R_{12} = -R_{21} \tag{29}$$

$$T_{12}T_{21} - R_{21}R_{21} = T_{12}T_{21} - R_{12}(-R_{12}) = T_{12}T_{21} + R_{12}^2 = T + R = 1 \tag{30}$$

Finally, substituting Eqs. (30) in (28), the (31) it is obtained for the net amplitude reflected thermal wave in to medium 3.

$$R_T = \frac{R_{12} + R_{23}e^{i\hat{\beta}}}{1 - R_{21}R_{23}e^{i\hat{\beta}}}$$
$$= \frac{[\xi_{12}(1 - \xi_{23})] \cdot (1 + e^{-2d/\delta}) + (\xi_{23} - \xi_{12}^2) \cdot (1 - e^{-2d/\delta})}{[\xi_{12}(1 + \xi_{23})] \cdot (1 + e^{-2d/\delta}) + (\xi_{23} + \xi_{12}^2) \cdot (1 - e^{-2d/\delta})} \tag{31}$$

A similar calculation gives the net amplitude transmitted thermal wave in medium 3; the Eq. (32) is obtained.

$$T_T = \frac{T_{12}T_{23}e^{i(\hat{\beta}/2)}}{1 - R_{21}R_{23}e^{i\hat{\beta}}}$$
$$= \frac{2 \cdot \{\xi_{23} + \xi_{12}[1 + (1 + \xi_{12}) \cdot e^{-d/\delta}]\}}{[\xi_{12}(1 + \xi_{23})] \cdot (1 + e^{-2d/\delta}) + (\xi_{23} + \xi_{12}^2) \cdot (1 - e^{-2d/\delta})} \tag{32}$$

Modulated Incident Light Beam

The light intensity at the material surface is the light energy per area per unit time from a sinusoidal modulated monochromatic light source is expressed as Eq. (33).

$$I_S = \text{Re}\left[\frac{I_0}{2}(1 + e^{i\omega t})\right] = \text{Re}\left[\frac{I_0}{2}(1 + \text{Cos}(\omega t) + i \cdot \text{Sin}(\omega t))\right]$$
$$= \frac{I_0}{2}[1 + \text{Cos}(\omega t)] \tag{33}$$

It is defined the heat density generated per time (H) as energy per time per unit of length per unit area, produced at any level depth profile z due to the light absorbed at that level is defined by Eq. (36), where interested in the change in light intensity from surface to same depth (z), since the charge increment in a thin thickness sample (Δz) at a depth

(z) is proportional to the light intensity (I) at depth z (Iz) and the slice thickness (Δz) the Eqs. (34) and (35) is obtained, where β is the proportionally constant.

$$\Delta I_z = I_z - I_{(z+\Delta z)} = \beta \cdot I_z \Delta_z, \; \beta = \frac{\Delta I_z}{I_z} \cdot \frac{1}{\Delta z}, \frac{\Delta I_z}{I_z} = \beta \cdot \Delta z \tag{34}$$

$$\int_{I_0}^{I_z} \frac{dI}{I} = \beta \cdot \int_0^z z, \; \ln\left(\frac{I_z}{I_0}\right) = \beta \cdot z, I_z = I_0 e^{\beta \cdot z} \tag{35}$$

$$H = \beta \cdot I_z = \beta \cdot I_0 e^{\beta z} = \beta\left\{\frac{I_0}{2}[1 + \text{Cos}(\omega t)]\right\}e^{\beta z}$$
$$= \frac{I_0 \cdot \beta \cdot e^{\beta z}}{2}[1 + \text{Cos}(\omega t)] \tag{36}$$

From Eq. (39) the heat density generated per time (H) is the absorption coefficient (β) per light energy per area per time (Iz) has assumed that light all is converted into heat, but are processes as electron–hole dissociation, chemical changes so that only part goes into generating the heat in thermal wave, this implies that another constant (η) introduced in Eq. (36) which is the efficiency at which the absorbed light at wavelength (λ) is converted to heat by non-radioactive excitation processes: Incorporating this efficiency is obtained the Eq. (37).

$$H = \text{Re}\left[\frac{I_0 \cdot \eta \cdot \beta \cdot (1 + e^{i\omega t}) \cdot e^{\beta z}}{2}\right] = \frac{I_0 \cdot \eta \cdot \beta \cdot [1 + \text{Cos}(\omega t)] \cdot e^{\beta z}}{2} \tag{37}$$

From Eqs. (8) and (37), there is an adjustment in the equation for the heat energy increase rate in a given volume from Fig. 4, equals the heat flux entering through the volume surface element plus the heat energy deposited per time by the light that is defined by Eqs. (38) and (39).

$$\int_{z_1}^{z_2} dz\left[c\rho\left(\frac{d\Phi}{dt}\right) - \kappa\left(\frac{d\Phi^2}{dz^2}\right) - H\right] = 0,$$
$$\kappa\left(\frac{d\Phi^2}{dz^2}\right) = c\rho\left(\frac{d\Phi}{dt}\right) - H \tag{38}$$

$$\frac{d\Phi^2}{dz^2} = \frac{c\rho}{\kappa_s}\left(\frac{d\Phi}{dt}\right) - \frac{H}{\kappa_s} = \frac{1}{\alpha_s}\left(\frac{d\Phi}{dt}\right) - \left(\frac{\beta \cdot I_0 \cdot \eta}{2 \cdot \kappa_s}\right) \cdot e^{\beta z} \cdot (1 + e^{i\omega t}) \tag{39}$$

Another adjustment is the solution real part to the Eq. (39), the differential equation represents the temperature in the sample relative to the ambient temperature (Φ0) as position function (z) and time (t). The actual temperature field in the sample is given by Eq. (40).

$$T(z, t) = \text{Re}al.Part.\Phi(z, t) + ambient = \text{Re}[\Phi(z, t)] + \Phi_0 \tag{40}$$

Depth Profile Thermal Wave

In general, from the point of view optical material is characterized by optical opacity, which is determined by the relationship between the optical absorption length ($\mu\beta =1/$ aj) and the material thickness (l), where the skin depth (δ) is important because is the maximum depth when the beam modulation frequency is zero. So according to the optical opacity, the solids can be divided into two groups, the first case is when optically transparent, when all the light intensity reaching the surface thereof a small part is absorbed throughout the specimen thickness, but most is transported is show in Fig. 6. This is expressed mathematically as μs>l. The second case is when it is optically opaque, when the light intensity reaching the solid surface is attenuated completely long before passing through the sample, it is written μs>>l. Furthermore, since the thermally solid it can be classified according to the relationship between the magnitude of the thermal diffusion length, defined as μs and thickness of the sample is according to Eq. (41) is show in Fig. 6 and defined units for photoacoustic parameters in Table 1.

$$\sigma_j = (1 + i) \cdot a_j, a_j = \sqrt{\frac{\omega}{2 \cdot \alpha_j}} = \sqrt{\frac{\pi \cdot f}{\alpha_j}} = \frac{1}{\mu_j},$$
$$\mu_s = \sqrt{\frac{2 \cdot \kappa}{c \cdot \rho \cdot \omega}} = \sqrt{\frac{\alpha_s}{\pi \cdot f}} \tag{41}$$

Photoacoustic Cell Model

Additionally, Fig. 7 shows the electromagnetic functionality model based on the basic components of a microphone. The photoacoustic theory cell involves open microphone cross section as shown in Fig. 7 and uses parameters from Table 1, in which the electret foil having a charge density, dielectric constant σ0 with thickness lm and separate metal support an air thickness s1, there is also a voltage V due to resistive load R it is generating an electric field E, that the applied air is called E0 where εR= 1.00051≈1 and ε0=8.8541878176×10–12 F/m are used for the permittivity. If a wave hits periodically changing electrical fields and charges indicated in the dielectric plates, applying Gauss theorem at the electret interface and the air chamber and between the bladder and support, using Eq. (42) and obtained.

$$\varepsilon_0 E_0 = \sigma_i, \varepsilon E - \varepsilon_0 E_0 = \sigma_0 \tag{42}$$

The induced surface charge density is we can relate it to V by Ohm's Law (V = IR) is expressed as Eq. (43), where A represents the support area.

$$V = R \cdot A \cdot (d\sigma / dt) = R \cdot A \cdot \varepsilon \left(dE_0 / dt \right) \tag{43}$$

Now try to find E of Fig. 7 are f(x) and F(x) electrical potentials in the electret (0 <x <lm) and the air chamber [lm <x < (lm + s1)] as a capacitors pair connected in parallel. The fields in these regions are constant and potential are lines, the potential differences between the metal plate that covers the electret and the metal bracket is written as Eqs. (44).

$$V = -\left(E_0 \cdot S_1 + E \cdot l_m\right), E_0 = \left(\varepsilon \cdot V + l_m \cdot \sigma_0\right) / \left(l_m \cdot S_0 + S_1 \cdot \varepsilon\right) \tag{44}$$

Differentiating the Eq. (44) with respect to time (rate) and using the result in Eq. (43) get differential equations for V which is defined as Eq. (45), where C is the capacitance microphone.

Fig. 6 Illustration thermally thick and thermally thin behavior with respect to incident wave front
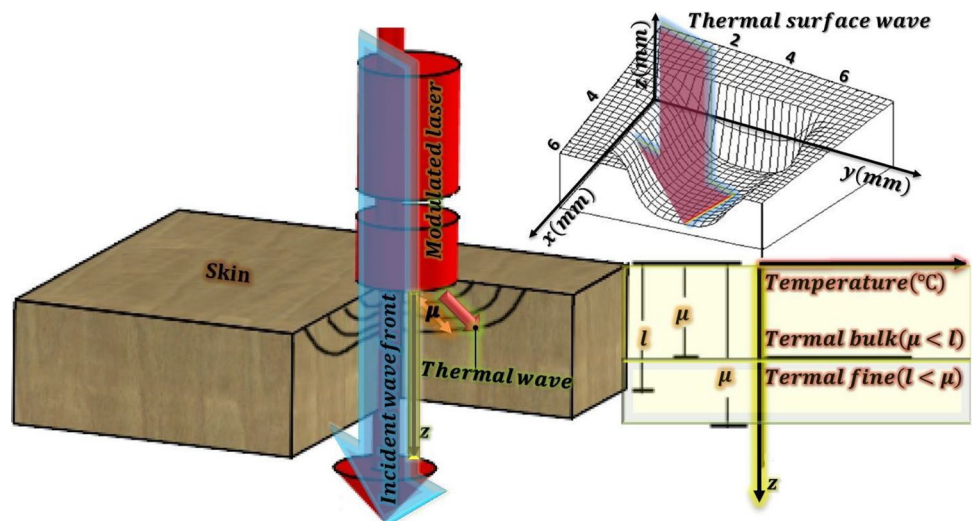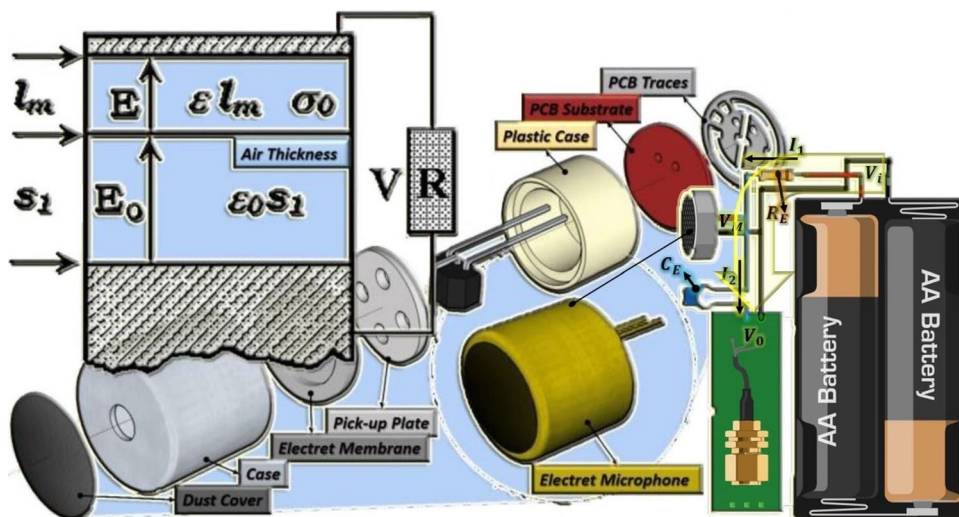
Table 1 Units for photoacoustic parameters

Parameter	Denomination	Units
K_j	Material thermal conductivity j	w/cm-K
ρ_j	Material density j	gr/cm3
C_j	Material specific heat j	w/g-K
Ω	Incident light beam modulation frequency	hertz (Hz)
α_j	Material thermal diffusivity j	cm2/sec
A_j	Material thermal diffusion coefficient j	cm^{-1}
O_j	Complex thermal diffusion coefficient j	cm^{-1}
$\mu j = 1a_j$	Material thermal diffusion length j	cm
L_s	Sample thickness	cm
L_b	Support thickness	cm
L_g	Gas column thickness	cm
β	Optical absorption coefficient	cm^{-1}
μ_β	Optical absorption length	cm
T	Time	seconds (sec)
Θ	Phase difference	degrees (°)
Φ_1	Specific heat of region 1	cal/gr–°C
e_1	Effusivity of region 1, $\sqrt{(\kappa_1 \rho_1 c_1)}$	cal/cm^2–°C–$\sqrt{sec}$
H	Efficiency at which the absorbed light wavelength is converted to heat	Arbitrary units (A.U.)
Γ	Specific heats radio of the constant pressure and at constant volume	Arbitrary units (A.U.)
ξ_{12}	Effectivities of side 2 and side 1	Arbitrary units (A.U.)
T_{12}	Thermal wave transmission coefficient from region 1 to region 2	Arbitrary units (A.U.)
R_{12}	Thermal wave reflected coefficient from region 1 to region 2	Arbitrary units (A.U.)

Fig. 7 Electret microphone section and physical characteristics for Photoacoustic, connections with passive electrical components schematic

$$\left(\frac{dV}{dt}\right) \cdot R \cdot C + V \cdot \left[1 - \frac{R \cdot C}{l_m \cdot \varepsilon_0 + S_1 \cdot \varepsilon}\left(\frac{dS_1}{dt}\right)\right]$$
$$= R \cdot C \cdot \left[\frac{l_m \cdot \sigma_0}{l_m S_0 + S_1 \varepsilon}\left(\frac{dS_1}{dt}\right)\right], C = \frac{A\varepsilon\varepsilon_0}{l_m S_0 + S_1 \varepsilon} \quad (45)$$

Due to the diaphragm reflection by the sound (S_1) is given by Eq. (46), where reflection diagram ($e^{i\omega t}$) is caused by pressure ($\delta P e^{i\omega t}$).

$$S_1 = l_b + \eta e^{i\omega \cdot t}, dS_1 / dt = i\omega \eta \cdot e^{i\omega \cdot t} \quad (46)$$

Substituting Eqs. (46) in (45), the Eq. (47) is obtained.

$$\frac{dV}{dt} + V \cdot \left(\frac{1}{RC} - i\frac{\omega \cdot \eta \cdot e^{i\omega t}}{l_m \varepsilon_0 + S_1 \varepsilon}\right) = i\frac{\omega \cdot \eta \cdot l_m \cdot \sigma_0 \cdot e^{i\omega t}}{l_m S_0 + S_1 \varepsilon} \quad (47)$$

From Eqs. (46), if assume that $\eta \ll lb$, Eq. (47) is reduced Eq. (48), where VM is Voltage Microphone.

$$\frac{dV_M}{dt} + \frac{V_M}{RC} = i\frac{\omega \cdot \eta \cdot l_m \cdot \sigma_0 \cdot e^{i\omega t}}{l_m S_0 + S_1 \varepsilon} \tag{48}$$

Finality from Eq. (48), the solution to the differential equation represented by Eq. (49).

$$\begin{aligned} V_M &= \left(\frac{i \cdot \omega \eta RC}{1 + i\omega RC}\right)\left(\frac{l_m \cdot \sigma_0}{l_m S_0 + S_1 \varepsilon}\right)e^{i\omega t} \\ &= \left(\frac{(\omega\tau)^2}{1 + (\omega\tau)^2} + i\frac{\omega\tau}{1 + (\omega\tau)^2}\right)\left(\frac{\eta \cdot l_m \cdot \sigma_0}{l_m S_0 + S_1 \varepsilon}\right)e^{i\omega t}, \tau = RC \end{aligned} \tag{49}$$

From Eq. (49), is the microphone output voltage when the diaphragm is subjected to harmonic fluctuations. We can identify this equation equivalent electret microphone circuit is an RC circuit in parallel with a power proportional to the current reflection microphone change rate (τ). The membrane displacement can solve a motion equation for a circular membrane extended, under tension T. This is the model (Kettel-Drum model) for electret microphone. The membrane movement compresses and expands the air from the chamber located behind the diaphragm and it reacts in the opposite direction to the membrane movement by changing its natural frequency and general behavior. If the wave velocity is considerably less than the sound speed in the air, then the compression and air expansion in the chamber is roughly the same over the entire membrane and depends on the average displacement of this. Considering the reaction force, also as the drag force due to the sound pressure, the sound motion equation is written as Eq. (50), where M is the mass per unit area of the membrane, PgVg is the air density (sound velocity).

$$M\frac{\partial^2 \eta}{\partial t^2} = T \cdot \nabla^2 \eta + \delta \cdot Pe^{i\omega t} - \frac{P_g V_g}{l_b}\eta \tag{50}$$

The temperature fluctuation in the system displays gas-chamber-membrane is obtained from the solution of the diffusion equations in the same system, solving Eq. (50) and considering only frequencies well below resonance Eq. (51) is obtained, where P is the ambient pressure, and γ the specific heats ratio.

$$\eta = l_b\left(\delta P / \gamma P_0\right) \tag{51}$$

Substituting Eqs. (51) in (49), Eqs. (52) and (53) is finally obtained and parameter is show in Fig. 7.

$$\begin{aligned} V_M &= \left[\frac{\omega\tau(\omega\tau + i)}{1 + (\omega\tau)^2}\right]\left(\frac{l_m \cdot l_b \cdot \sigma_0}{l_m S_0 + S_1 \varepsilon}\right)\left(\frac{\delta P}{\gamma P_0}\right) \cdot e^{i\omega t} \\ &= \left[\frac{\omega\tau(\omega\tau + i)}{1 + (\omega\tau)^2}\right] \cdot V_0 \cdot e^{i\omega t} \end{aligned} \tag{52}$$

$$V_0 = \left(\frac{l_m \cdot l_b \cdot \sigma_0}{l_m S_0 + S_1 \varepsilon}\right)\left(\frac{\delta P}{\gamma P_0}\right) \tag{53}$$

From Fig. 7, using Ohm's Law and Kirchhoff current law, the Eqs. (54–56) is obtained.

$$I_1 = \frac{V_i - V_M}{R_E} \tag{54}$$

$$I_2 = i\omega C_E\left(V_M - V_0\right) \tag{55}$$

$$I_1 = I_2 \tag{56}$$

Substituting Eqs. (54) and (55) in (56), the function described by Eq. (57) is obtained.

$$V_i = \left(1 + i\omega R_E C_E\right)V_M - i\omega R_E C_E V_0 = R_E C_E \tag{57}$$

Substituting Eqs. (52) in (57), the transfer function described by Eq. (58) is obtained.

$$\begin{aligned} H(i\omega) &= \frac{V_0}{V_i} = \frac{\omega\tau\left[e^{i\omega t}\left(\omega\tau_E + 1\right) - 1\right] - 1}{1 + \omega^2\tau^2\left[e^{i\omega t}\left(\omega\tau_E + 1\right) - 1\right]^2} \\ &\quad + i\frac{\omega\tau\left[e^{i\omega t}\left(\omega\tau_E + 1\right) - 2\right]}{1 + \omega^2\tau^2\left[e^{i\omega t}\left(\omega\tau_E + 1\right) - 1\right]^2} \end{aligned} \tag{58}$$

Results and Discussion

Calculating the magnitude and angle of the transfer function described by Eq. (58), is represented by Eqs. (59) and (60) respectively.

$$G(i\omega) = |H(i\omega)|^2 = \left[\sqrt{\left(\frac{K-1}{1+K^2}\right)^2 + \left(\frac{K-\omega\tau}{1+K^2}\right)^2}\right]^2 \tag{59}$$

$$\Theta(i\omega) = arc \cdot tg\left\{\frac{K - \omega \cdot \tau / \left[1 + K^2\right]}{K - 1 / \left[1 + K^2\right]}\right\} = arc \cdot tg\left(\frac{K - \omega\tau}{K - 1}\right) \tag{60}$$

From Eq. (58), to define the locus according to Eqs. (59) and (60) is calculated by considering the vector module ends G ($i\omega$) and the vector argument ends $\Theta(i\omega)$ by varying the frequency ω from 0 to 100,000 (khz.), which generates Table 2, where the lowpass filter both the external microphone and have a cutoff frequency of 600 kHz and occurs when there is a phase shift of 90°. The use of Eq. (59) and (60) experientially, the magnitude and phase of the signal are usually measured with lock-in amplifier, this instrument can have selected an interest frequency out a noisy incoming time simulation, it converts this time variating into continuous output levels available as meter

Table 2 Table values for represent the transfer function response H (iω) in the Bode plot

| Frequency (kHz)	Gain (G)	Time (Radians/Sec.)	Gain (Decibel dB)	Phase shift (Degrees°)
1	120.000336	104.72	41.5836487	−0.00191083
2	120.001335	209.44	41.5837212	−0.0038217
3	120.002998	314.16	41.5838432	−0.00573263
4	120.005333	418.88	41.5840111	−0.00764365
5	120.008331	523.6	41.5842285	−0.0095548
6	120.012001	628.32	41.5844917	−0.01146611
7	120.016335	733.04	41.5848083	−0.01337762
8	120.021332	837.76	41.5851669	−0.01528934
9	120.027	942.48	41.5855789	−0.01720132
590	3119.83716	61,784.8	69.882637	−30.7665005
591	3361.14966	61,889.52	70.5297546	−33.5068016
592	3632.92383	61,994.24	71.2051239	−36.7035294
593	3937.43237	62,098.96	71.9042587	−40.4553337
594	4274.69238	62,203.68	72.6180954	−44.8784981
595	4640.06689	62,308.4	73.3304825	−50.1017189
596	5020.62256	62,413.12	74.015152	−56.249897
597	5390.82422	62,517.84	74.6331024	−63.4096489
598	5710.18555	62,622.56	75.1330032	−71.5727234
599	5928.1123	62,727.28	75.4583282	−80.5709
600	6000	62,832	75.5630264	−89.9544907
601	5908.64648	62,936.72	75.4297638	−99.4138718
602	5674.12695	63,041.44	75.07798	−108.370201
603	5342.51416	63,146.16	74.5549164	−116.475922
604	4964.28662	63,250.88	73.9171371	−123.573906
605	4578.97363	63,355.6	73.2153625	−129.663498
606	4211.03955	63,460.32	72.4877853	−134.835007
607	3872.57007	63,565.04	71.7599869	−139.21431
608	3567.6311	63,669.76	71.0475998	−142.929657
609	3295.85303	63,774.48	70.3593597	−146.09639
610	3054.7561	63,879.2	69.6995316	−148.812027
6591	1.00275397	690,209.52	0.02388783	−179.89476
6592	1.00244725	690,314.24	0.02123055	−179.894775
6593	1.00214064	690,418.96	0.0185735	−179.894791
6594	1.00183415	690,523.68	0.01591667	−179.894806
6595	1.00152779	690,628.4	0.01326006	−179.894821
6596	1.00122166	690,733.12	0.0106047	−179.894836
6597	1.00091553	690,837.84	0.00794853	−179.894852
6598	1.00060964	690,942.56	0.00529362	−179.894867
6599	1.00030386	691,047.28	0.00263893	−179.894882

indications. The measure a time varying signal with a lock-in amplifier when measure a signal is expressed as Eq. (61).

$$S_{PA}(\omega_0) = M \cos\Theta \cos[\omega_0 t] + M \sin\Theta \cos[\omega_0 t + 90°] \tag{61}$$

where Eq. (61), the coefficient M*Cos(Θ) is the in-phase lock-in output and M*Sin(Θ) which is the coefficient of Cos(ωt+90°) is the quadrature output, where Cos(ωt+90°) is 90° phase out with the in-phase Cos(ωt). The lock-in output corresponds to the incoming signal magnitude at the reference signal frequency and also at a given phase angle with respect to the reference signal, the projection vector representing the signal on an axis or instrument phase. The magnitude may be calculated from the square root of the squares sum of the in-phase and quadrature outputs calculating the magnitude from real and imaginary parts of a complex number or converting from rectangular to cylindrical coordinates. The signal is the complexity of a complex

Fig. 8 Graph absorption spectrum for oxyhemoglobin (HbO2) deoxyhemoglobin (Hb) and region of the spectrum where the blue and green lasers interacts
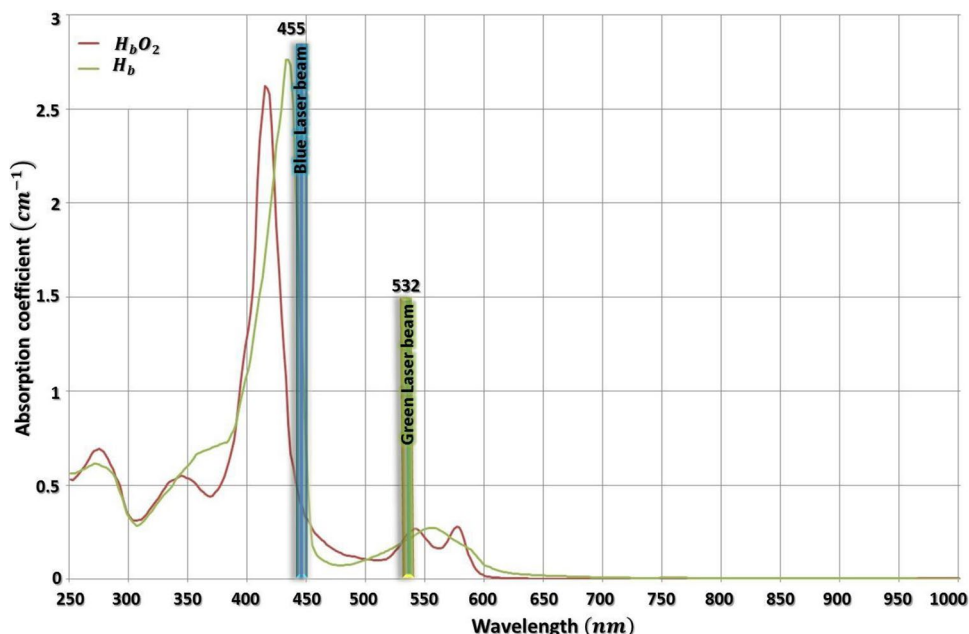
number expression; it can be expressed as a real numbers pair can be written as Eq. (62).

$$\psi = a + ib = re^{i\theta} = \sqrt{a^2 + b^2}e^{i\left[tg^{-1}(b/a)\right]} \tag{62}$$

From Eq. (62), the magnitude and phase is obtained from an expression ψ can be written as Eqs. (63) and (64) respectively.

$$r = \sqrt{a^2 + b^2} = \sqrt{\psi \cdot \psi^*} \tag{63}$$

$$\theta = tg^{-1}(b/a) = tg^{-1}\left[(\psi - \psi^*)/i \cdot (\psi + \psi^*)\right] \tag{64}$$

From Fig. 8, the absorption coefficient (α) is a function of the wavelength α(λ). This factor is very important to understand the interaction of electromagnetic radiation with matter in most laser applications and the customary measurement unit in the spectroscopy literature is 1/cm or cm^{-1}. Moreover, the graph of Fig. 8, shown the absorption spectrum for oxy-hemoglobin (HbO2) deoxy-hemoglobin (Hb) and region of the spectrum where the blue and green lasers interacts, where two peaks, one for a blue laser (445 nm) and green laser (532 nm) are presented in the absorption spectrum, therefore, for this project it was taken into account because blue laser as shown in Fig. 8 has higher absorption of light intensity green laser in the blood deoxy-hemoglobin case. At these wavelengths optical measurements take advantage by instruments called oximeters, which obtained the oxygen percentage in the blood and heart pressure, but unfortunately the thermal part is not considered, making it impossible to associate the optical and thermal properties for other important parameters within the blood. From Fig. 8,

the optical absorption spectrum, we have the following cases the hemoglobin molecule is bound to oxygen then one has oxy-hemoglobin (Hb02), the hemoglobin molecule is bound to carbon monoxide then one has carboxy-hemoglobin (HbCO), the hemoglobin molecule is bound to nothing then one has deoxy-hemoglobin (Hb), finally the hemoglobin molecule has broken down then one has met-hemoglobin. From Eq. (31), the reflection is defined between the skin surface (ξ12) is defined according to different skin color type, whereby measurements for six different skin types are made, measurements amplitude and phase are shown in Fig. 9, in the amplitude case, the dark skin color has a higher absorption, this measurement is compensated in the signal phase, allowing recover signals by phase sensitive amplifier, this same process is repeated for the other colors, the in any case allowing measure thermal wave properties in blood hemoglobin. In this regard, measurements being approved for any skin color type, it proceeds to measure hemoglobin in blood with different oxygen concentrations, the experimental results shown in Fig. 10, where hemoglobin measurement in the blood is possible because the amount lost as the photoacoustic signal amplitude is recovered as the wave phase, this process is replicated with different oxygen concentrations in different skin colors, this allows estimate thermal wave properties in blood hemoglobin.

Conclusions

A model-based formulation based on the heat equation solution to the wave equation in frequency domain was proposed. The method entails measuring the amplitude and phase for

Fig. 9 Graphing amplitude and phase of six different skin types to different modulation frequencies
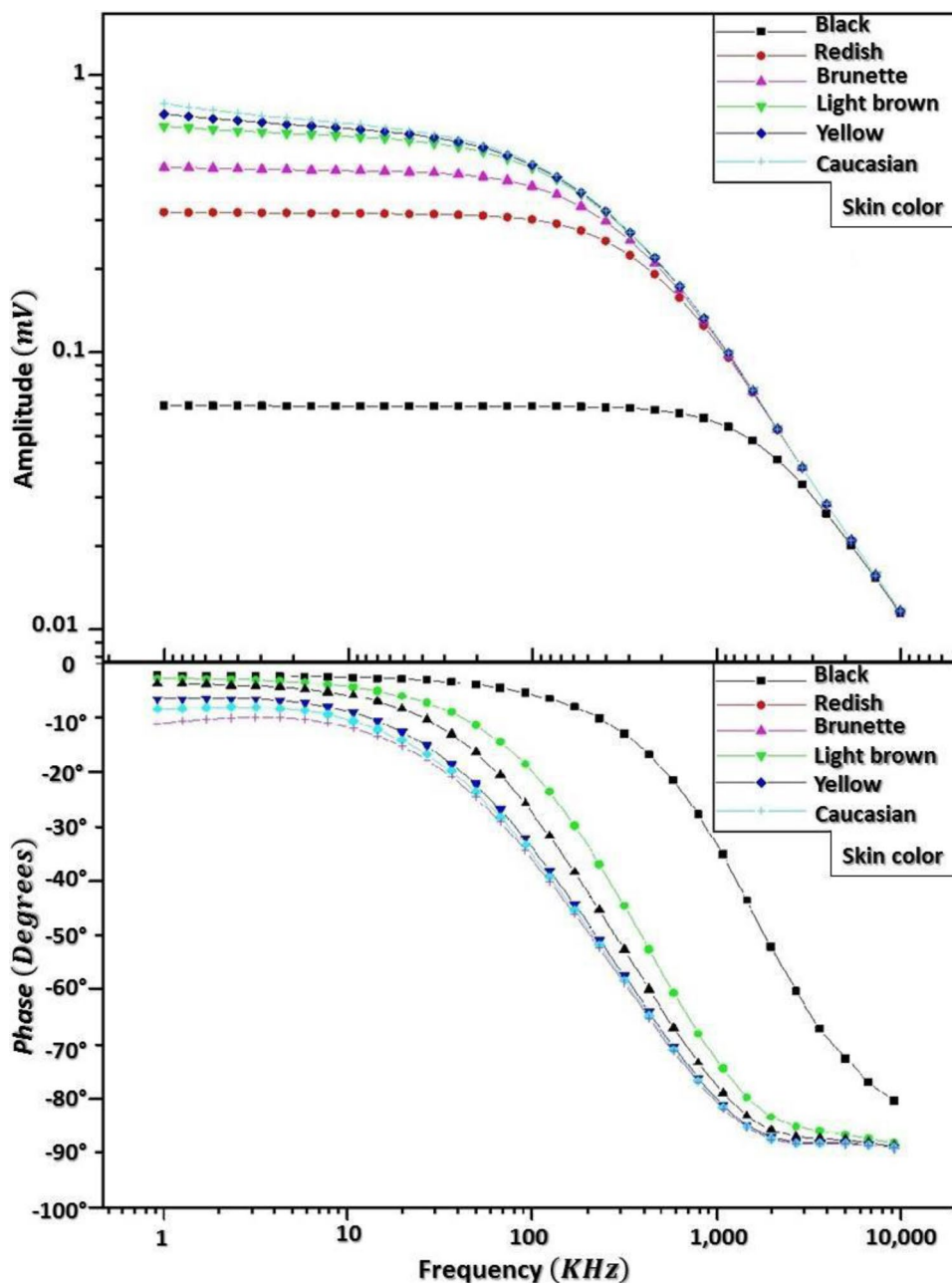
photoacoustic originating from a subcutaneous tissue subsurface absorber as a skin surface light spot is translated laterally by describe a reflection-mode photoacoustic method which permits estimation of thermal properties oxyhemoglobin and deoxyhemoglobin performed on fitting three surfaces in heat equation model using thermal wave interference approach. The results to be obtained are of high precision because, contrary to conventional methods, every measured coefficient is calculated by fitting the photoacoustic signal profile consist the amplitude and phase measurements on thermal depth profile generated by the change in the modulation frequency and are obtained a nanometer resolution. The model takes into account for changes in the thermal wave attenuation by different skin color types, for transmission and reflection at coefficients interfaces with sharply different boundaries optical interaction for potential reflected thermal waves off the subcutaneous tissue structure that might reach the detector. The reflection-mode photoacoustic measurements of a blood veins can be conducted at blue wavelength, allowing the oxygen saturation of the blood hemoglobin in the hand finger veins to be determined. Simulations at blue wavelength can indicate the sensitivity of a skin color photoacoustic measurement, allowing determine to the blood hemoglobin oxygen saturation through vein draining thermal

Fig. 10 Graphing amplitude and phase of different oxygen concentrations in blood hemoglobin to different modulation frequencies
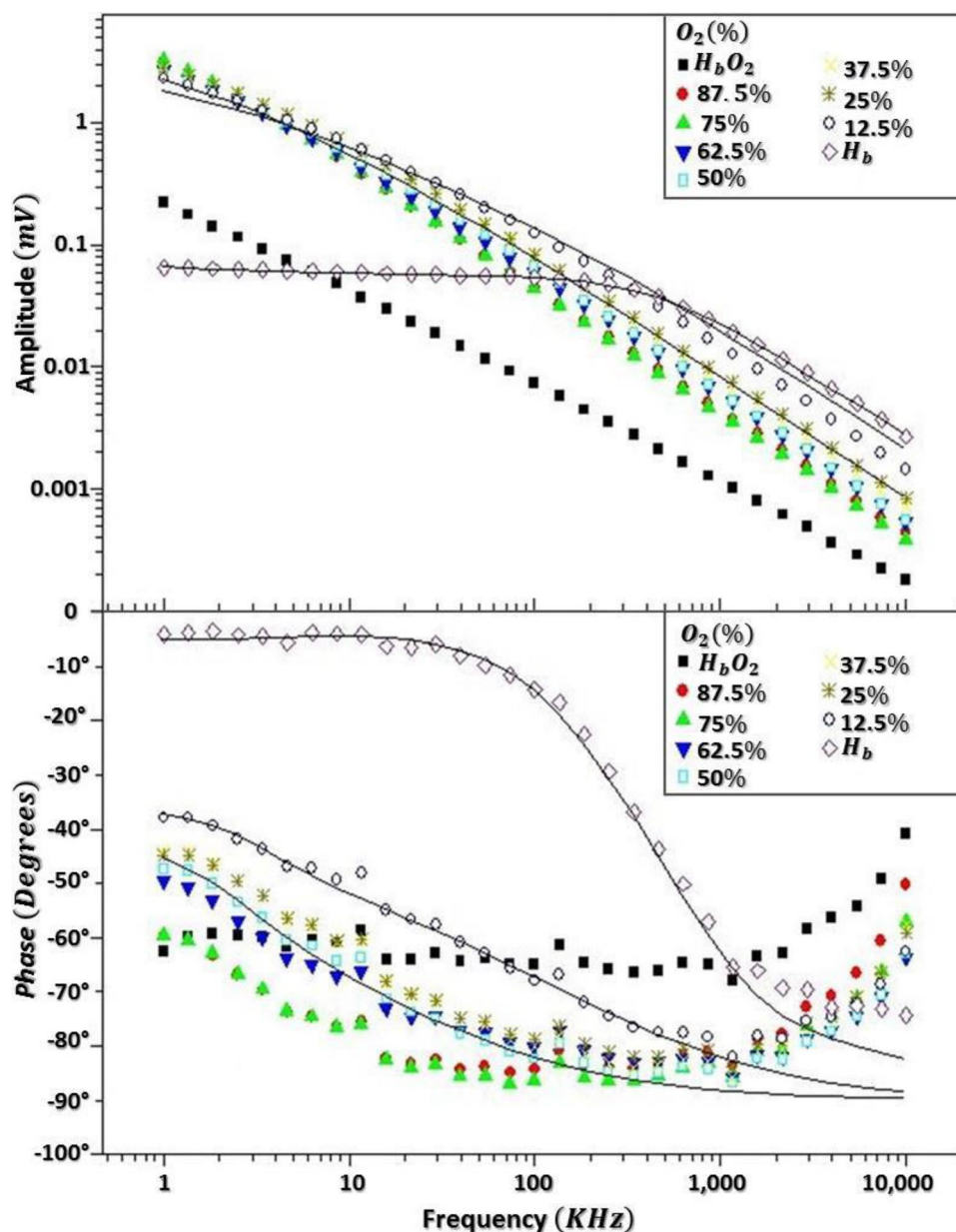
wave measurements a subcutaneous tissue will reveal the oxygen extraction by the hand finger tissue. The simulations results were presented for different skin color type data obtained from hand finger measurements. As the signal-generation theory and data gathering algorithms are embedded reflection-mode photoacoustic can be easily automated, and the embedded system setup has a simple and handy design, the mechanical and electronic components cost, as well as the methodology is used to work in the reflection-mode photoacoustic modeling which it is used as a tool inexpensive with respect to commercial equipment. Thus, future research should focus on designing and evaluating the performance of a model designed for this purpose and optimal system design based on development of specific trade-off schemes between

various system parameters is the next logical step of future work. These kinds of non-intrusive methods study as blood gas measurement, could also avoid degradation of the skin and the needle prick pain to obtain blood in the wrist vein and avoid blood contamination, due at the intrusion of external elements such as alcohol, virus, oxides, among other environmental pollutants. The heat equation model associated that a different skin color type measurement opens new problems in the photoacoustic theory in to estimate thermal wave properties in blood hemoglobin. According to Fig. 9, with the implementation of Eqs. (31) and (32), in the embedded reflection-mode photoacoustic system provide new opportunities to significantly increase measurement resolution in amplitude and phase which quantifies thermal

properties of single cells, viruses and bacteria in complex biological environments. From Fig. 10, we conclude that frequency domain photoacoustic may evolve to a practical experimental method using blue light intensity modulated sources using lock-in amplifier, with advantages over time-domain photoacoustic using spectrum analyzer. Thus, the model reflected pressure waves internally reflecting from the air/skin surface and encountering the skin/tissue and tissue/veins interfaces to reflect back toward the microphone detector selecting a proper wavelength for the application, a thermal depth profile resolution that does not involve dependences on the laser energy as in the optical properties case.

Data Availability All the data described is available from the authors, upon request.

Declarations

Conflict of interest None of the coauthors of this article have any conflict of interest, whatsoever.

References

1. M. Pawlak, M. Malinski, Noncontact measurement of the thermal diffusivity of IR semi-transparent and semiconducting n-CdMgSe mixed crystals by means of the photothermal radiometry. Infrared Phys. Technol. **64**, 87–90 (2014)
2. B. Arnala, C. Pereza, C. Weia, J. Xiaa, M. Lombardo, I. Pelivanov, T.J. Matula, L.D. Pozzo, M. O'Donnell, Sono-photoacoustic imaging of gold nanoemulsions: Part I. Exposure thresholds. Photoacoustics **3**(1), 26–34 (2015)
3. B. Arnala, C. Pereza, C. Weia, J. Xiaa, M. Lombardo, I. Pelivanov, T.J. Matula, L.D. Pozzo, M. O'Donnell, Sono-photoacoustic imaging of gold nanoemulsions: Part II. Real time imaging. Photoacoustics **3**(1), 26–34 (2015)
4. M. Srivalleesha, K. Seungsoo, K. Andrei, P.J. Pratixa, S. Konstantin, E. Stanislav, Visualization of molecular composition and functionality of cancer cells using nanoparticle-augmented ultrasound-guided photoacoustics. Photoacoustics **3**(1), 26–34 (2015)
5. V. Hanyecz, A. Mohácsi, S. Puskas, A. Vago, G. Szabo, Instrument for benzene and toluene emission measurements of glycol regenerators. Meas. Sci. Technol. **24**(11), 115901 (2013)
6. D. Tatrai, Z. Bozoki, H. Smit, C. Rolf, N. Spelten, M. Krämer, A. Filges, C. Gerbig, G. Gulyas, G. Szabo, Dual channel photoacoustic hygrometer for airborn measurements: background, calibration, laboratory and in-flight inter-comparison tests. Atmos. Meas. Tech. **8**, 33–42 (2015)
7. N. Utry, T. Ajtai, A. Filep, M. Pinter, Z.S. Torok, Z. Bozoki, G. Szabo, Correlations between absorption Angström exponent (AAE) of wintertime ambient urban aerosol and its physical and chemical properties. Atmos. Environ. **91**, 52–59 (2014)
8. Z. Filus, N. Toth, G. Gulyas, T. Guba, G. Szabo, Z. Bozoki, Carrier gas flow arrangement based photoacoustic detection method for measuring gas permeability of polymer membranes. Polym. Test. **32**(6), 1099–1104 (2013)
9. E. Tuboly, A. Szabo, G. Eros, A. Mohacsi, G. Szabo, R. Tengolics, G. Rakhely, M. Boros, Determination of endogenous methane formation by photoacoustic spectroscopy. J. Breath Res. **7**, 046004 (2013)
10. D. Tatrai, Z. Bozoki, G. Gulyas, G. Szabo, Embedded system based data acquisition and control system for photoacoustic spectroscopic applications. Measurement **63**, 259–268 (2015)
11. M. Chen, Y. He, J. Zhu, R. Kim, Enhancement of photo-thermal conversion using gold nanofluids with different particle sizes. Energy Convers. Manage. **112**, 21–30 (2016)
12. I. Sorrell, R.J. Shipley, V. Hearnden, H.E. Colley, M.H. Thornhill, C. Murdoch, S.D. Webb, Combined mathematical modelling and experimentation to predict polymersome uptake by oral cancer cells. Nanomed. Nanotechnol. Biol. Med. **10**, 339–348 (2014)
13. T.A. Filimonova, D.S. Volkov, M.A. Proskurnin, I.M. Pelivanov, Optoacoustic spectroscopy for real-time monitoring of strongly lightabsorbing solutions in applications to analytical chemistry. Photoacoustics **1**, 54–61 (2013)
14. O. Simandoux, A. Prost, J. Gateau, E. Bossy, Influence of nanoscale temperature rises on photoacoustic generation: Discrimination between optical absorbers based on thermal nonlinearity at high frequency. Photoacoustics **3**(1), 20–25 (2015)
15. X. Huang, M.A. El, Gold nanoparticles: Optical properties and implementations in cancer diagnosis and photothermal therapy. J. Adv. Res. **1**, 13–28 (2010)
16. M. Qu, M. Mehrmohammadi, R. Truby, I. Graf, K. Homan, S. Emelianov, Contrast-enhanced magneto-photo-acoustic imaging in vivo using dual-contrast nanoparticles. Photoacoustics **2**, 55–62 (2014)
17. K. Mitsuhashi, K. Wang, M.A. Anastasio, Investigation of the far-field approximation for modeling a transducer's spatial impulse response in photoacoustic computed tomography. Photoacoustics **2**, 21–32 (2014)
18. M. Sarimollaoglu, D.A. Nedosekin, Y.A. Menyaev, M.A. Juratli, V.P. Zharov, Nonlinear photoacoustic signal amplification from single targets in absorption background. Photoacoustics **2**, 1–11 (2014)
19. J.C. Ranasinghesagara, Y. Jiang, R.J. Zemp, Reflection-mode multiple-illumination photoacoustic sensing to estimate optical properties. Photoacoustics **2**, 33–38 (2014)
20. S.L. Jacques, Coupling 3D Monte Carlo light transport in optically heterogeneous tissues to photoacoustic signal generation. Photoacoustics **2**, 137–142 (2014)

21. P. Arpaia, E. Matteis, V. Inglese, Software for measurement automation: A review of the state of the art. Measurement **66**, 10–25 (2015)

22. T. Qiu, L. Feng, H. Jiang, W. Sun, Queueing model analysis and scheduling strategy for embedded multi-core SoC based on task priority. Comput. Electr. Eng. **39**, 24–33 (2013)

23. S. Khan, L. Finkelstein, Mathematical modelling in the analysis and design of hard and soft measurement systems. Measurement **46**, 2936–2941 (2013)

24. Z. Domotor, V. Batitsky, An algebraic–analytic framework for measurement theory. Measurement **43**, 1142–1164 (2010)

25. P. Neelamegam, A. Jamaludeen, A. Rajendran, Prediction of calcium concentration in human blood serum using an artificial neural network. Measurement **44**, 312–319 (2011)

26. P. Daponte, L. De Vito, F. Picariello, M. Riccio, State of the art and future developments of measurement applications on smart-phones. Measurement **46**, 3291–3307 (2013)

27. P. Mohajerani, S. Kellnberger, V. Ntziachristos, Frequency domain optoacoustic tomography using amplitude and phase. Photoacoustics **2**, 111–118 (2014)

28. J. Yao, L.V. Wang, Sensitivity of photoacoustic microscopy. Photoacoustics **2**, 87–101 (2014)

29. R.Z. Morawski, A. Miekina, Application of principal components analysis and signal-to-noise ratio for calibration of spectrophotometric analysers of food. Measurement **79**, 302–310 (2016)

30. T. Piasecki, K. Chabowski, K. Nitsch, Design, calibration and tests of versatile low frequency impedance analyser based on ARM microcontroller. Measurement **91**, 155–161 (2016)

31. A. Cifuentes, E. Marín, Implementation of a field programmable gate array-based lock-in amplifier. Measurement **69**, 31–41 (2015)

32. K. Strzałkowski, M. Streza, M. Pawlak, Lock-in thermography versus PPE calorimetry for accurate measurements of thermo-physical properties of solid samples: A comparative study. Measurement **64**, 64–70 (2015)

33. A. Kotze, Pre-optimization of the anaemic patient. Anaesthesia Intens. Care Med. **17**(2), 67–69 (2016)

34. M. O'Meara, M. Allford, Anaesthesia for patients with sickle cell and other haemoglobinopathies. Anaesthesia Intens. Care Med. **11**(6), 242–243 (2010)

35. F. O'Sullivan, M. Al, Acute respiratory distress syndrome. Anaesthesia Intens. Care Med. **14**(10), 472–474 (2013)

36. A.N. Davies, P. Saravanan, Tests of pulmonary function before thoracic surgery. Anaesthesia Intens Care Med **15**(11), 495–498 (2014)

37. S. Mahmood, Measurement of respiratory function: an update on gas exchange. Anaesthesia Intens Care Med **16**(2), 68–73 (2015)